

FLUSI: A NOVEL PARALLEL SIMULATION TOOL FOR FLAPPING INSECT FLIGHT USING A FOURIER METHOD WITH VOLUME PENALIZATION[¶]

THOMAS ENGELS^{*†‡} DMITRY KOLOMENSKIY[§] KAI SCHNEIDER[‡] AND JÖRN SESTERHENN[†]

Abstract. FluSI, a fully parallel open source software for pseudo-spectral simulations of three-dimensional flapping flight in viscous flows, is presented. The computational framework runs on high performance computers with distributed memory architectures. The discretization of the three-dimensional incompressible Navier–Stokes equations is based on a Fourier pseudospectral method with adaptive time stepping. The complex time varying geometry of flapping insects with rigid wings is handled with the volume penalization method. The modules characterizing the insect geometry, the flight mechanics and the wing kinematics are described. Validation tests for different benchmarks illustrate the efficiency and precision of the approach. Finally, computations of a model insect in the turbulent regime give an outlook of the versatility of the software.

Key words. Pseudospectral method, volume penalization; flapping insect flight

AMS subject classifications. 76M22, 65M85, 74F10, 76Z10, 65Y05, 76F65

1. Introduction. Flapping flight is an active interdisciplinary research field with many open questions, and numerical simulations have become an important instrument for tackling them. Here, we present a computational solution environment which is, to the best of our knowledge, the first open source code in this field¹. The framework can be applied to flapping flyers, e.g., insects and man-made micro air vehicles, but for simplicity we shall only focus on the former.

In the literature different numerical strategies have been proposed simulating flapping flight, e.g., the use of several, overlapping grids [24], that are adapted to the geometry, or the use of moving grids with the Arbitrary Lagrangian-Eulerian (ALE) method [37]. Those methods involve significant computational and implementation overhead, whose reduction has motivated the development of methods that allow for a geometry-independent discretization, such as immersed boundary methods.

In this work, we employ the volume penalization method to take the no-slip boundary condition into account. The idea of modeling solid obstacles as porous media with a small permeability has been proposed by Arquis and Caltagirone [2]. The forcing term acts on the entire volume of the solid and not only on its surface, as it is the case in the immersed boundary methods, and corresponds to the Darcy drag. The method’s distinctive feature is the existence of rigorous convergence proofs

[¶]This work was granted access to the HPC resources of Aix- Marseille Université financed by the project equip@meso (ANR-10-EQPX-29-01) of the program « investissements d’avenir » supervised by the Agence Nationale pour la Recherche, as well as to the HPC resources of IDRIS (Institut du Développement et des Ressources en Informatique Scientifique) under project number i20152a1664. TE,KS,JS thank the French-German University for financial support. The authors wish to thank Masateru Maeda for fruitful discussions.

^{*}Corresponding author, e-mail address: thomas.engels@mailbox.tu-berlin.de

[†]ISTA, Technische Universität Berlin, Müller-Breslau-Strasse 12, 10623 Berlin, Germany

[§]Biomechanical Engineering Laboratory, Chiba University, 1-33, Yayoi-cho, Inage-ku, Chiba-shi, Chiba, 263-8522, Japan

[‡]M2P2 UMR7340, CNRS and Aix-Marseille Université, 38 rue Joliot-Curie 13451 Marseille cedex 20, France

¹The FluSI (acronyme for FLUId Structure Interaction) code is freely available for non-commercial use under <https://github.com/pseudospectators/FLUSI>

[1, 7] showing that the solution of the penalized equations does indeed converge to the solution of the Navier-Stokes equations with no-slip boundary conditions. This approach has been extended to model not only Dirichlet conditions applied at the surface of moving, rigid and flexible obstacles [22, 11], but also to homogeneous Neumann conditions, which is relevant for studying, e.g., turbulent mixing of a passive scalar [18]. As animals forage following odor traces, this technique can potentially be attractive for insect flight simulations as well. Variants of the penalization method have been developed for compressible flow [5, 42, 25] and magneto-hydrodynamics [29, 30]. An interesting recent development has been proposed in [16] in the context of finite-difference discretizations. Their idea is to modify the fractional step projection scheme such that the Neumann boundary condition, as proposed by Kadoch et al. [18], appears in the pressure Poisson equation. Another variant, specifically adopted to impulsively started flow, is the iterative penalization method proposed in [15]. For reviews on immersed boundary and penalization techniques we refer to [28, 35, 40].

In the context of biolocomotion, the penalization method has, for example, been used to study the C-start of a fish at rest [14], which showed, using a genetic algorithm, that the observed, natural starting behavior is the best solution for this type of problem. An advantage of the penalization method is its simplicity in implementation and computation, which is a crucial prerequisite for the usage of genetic algorithms.

The remainder of this article is organized as follows. First we discuss in section 2 the numerical method of FluSI's fluid module, which is based on a spectral discretization of the three-dimensional penalized Navier-Stokes equations, and then its parallel implementation in section 3. Section 4 describes the module that creates the insect geometry, as well as the governing equations for free flight simulations. Thereafter we present a validation of our software solution environment in section 5 for different test cases established in the literature, and give an outlook for applications to flapping flight in the turbulent regime in section 6. Conclusions are drawn in section 7.

2. Numerical method.

2.1. Model equations. For the numerical simulation of flapping flyers, like insects, the fluid can typically be approximated as incompressible. It is thus governed by the incompressible Navier-Stokes equations

$$(2.1) \quad \partial_t \underline{u} + \underline{\omega} \times \underline{u} = -\nabla \Pi + \nu \nabla^2 \underline{u} + F_p \quad \underline{x} \in \Omega_f, t > 0$$

$$(2.2) \quad \nabla \cdot \underline{u} = 0$$

with the no-slip boundary condition

$$(2.3) \quad \underline{u}|_{\partial\Omega_s(s,t)}(s,t) = \underline{u}_s(s,t)$$

and the initial condition

$$(2.4) \quad \underline{u}(\underline{x}, t=0) = \underline{u}_0(\underline{x})$$

where \underline{u} is the fluid velocity, $\underline{\omega} = \nabla \times \underline{u}$ is the vorticity, ν is the kinematic viscosity and F_p is an external force, usually a pressure gradient. Eqns. (2.1-2.4) are written in dimensionless form and the fluid density ϱ_f is normalized to unity. The nonlinear term in eqn. (2.1) is written in the rotational form, hence one is left with the gradient of the total pressure $\Pi = p + \frac{1}{2} \underline{u} \cdot \underline{u}$ instead of the static pressure p [36]. This formulation is chosen because of its favorable properties when discretized with spectral methods, namely conservation of momentum and energy [36, pp. 210]. A sketch of the problem

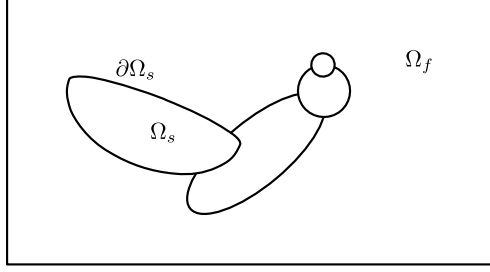


FIGURE 2.1. Domain definitions. Solid obstacles Ω_s (e.g., an insect) immersed in a fluid domain Ω_f . The computational domain is $\Omega = \Omega_f \cup \Omega_s$.

is given in figure 2.1. The no-slip boundary condition, eqn. (2.3), is satisfied on the fluid–solid interface $\partial\Omega_s$, which moves with velocity \underline{u}_s . At the exterior of the computational domain Ω , which is supposed to be sufficiently large, periodic boundary conditions can be assumed.

The numerical solution of eqns. (2.1-2.4) poses two major challenges. The most severe difficulty is the fact that the pressure Π is not a thermodynamic variable satisfying an equation of state, but rather a Lagrangian multiplier that ensures the divergence-free condition (2.2). In addition, the boundary condition (2.3) must be satisfied on a possibly complicated and moving fluid–solid interface. Traditional numerical approaches rely on boundary-fitted grids and fractional step methods [19], requiring to solve a Poisson problem for the pressure, to cope with these difficulties. Since the generation of boundary-fitted grids for complicated geometries is a challenging problem on its own [44], which possibly has to be repeated at every time step, alternatives have been developed. The principal idea is to extend the computational domain to the interior of obstacles as well, i.e., $\Omega = \Omega_f \cup \Omega_s$ in figure 2.1. The boundary is then taken into account by adding supplementary terms to equation (2.1). The approach chosen here is the volume penalization method, which is physically motivated by replacing the solid obstacle Ω_s by a porous medium with small permeability C_η . The penalized version of the Navier–Stokes equations reads

$$(2.5) \quad \partial_t \underline{u} + \underline{\omega} \times \underline{u} = -\nabla \Pi + \nu \nabla^2 \underline{u} + F_p - \frac{\chi}{C_\eta} (\underline{u} - \underline{u}_s) \quad \underline{x} \in \Omega, t > 0$$

$$(2.6) \quad \nabla \cdot \underline{u} = 0$$

$$(2.7) \quad \underline{u}(\underline{x}, t = 0) = \underline{u}_0(\underline{x}).$$

Note that in the fluid domain Ω_f one recovers the original equation as the penalization term $\frac{\chi}{C_\eta} (\underline{u} - \underline{u}_s)$ vanishes. The convergence proof in [7, 1] shows that the solution of the penalized Navier–Stokes equations (2.5-2.7) tends for $C_\eta \rightarrow 0$ indeed towards the exact solution of Navier–Stokes imposing no-slip boundary conditions (2.1-2.4), with a convergence rate of $\mathcal{O}(\sqrt{C_\eta})$ in the L^2 -norm. The parameter C_η should thus be chosen to a small enough value. The mask function χ is defined as

$$(2.8) \quad \chi(\underline{x}, t) = \begin{cases} 0 & \text{if } \underline{x} \in \Omega_f \\ 1 & \text{if } \underline{x} \in \Omega_s \end{cases}.$$

In anticipation of the application to moving boundaries, we note that we will replace the discontinuous χ -function by a smoothed one, with a thin smoothing layer centered around the interface. The mask function encodes all geometric information of the

problem, and eqns. (2.5-2.7) do not include no-slip boundary conditions; at the outer boundary $\partial\Omega$, periodicity is assumed. The aerodynamic force \underline{F} and the torque moment \underline{m} can be computed from

$$(2.9) \quad \underline{F} = \oint_{\partial\Omega_s} \sigma \cdot \underline{n} \, d\gamma = \frac{1}{C_\eta} \int_{\Omega} \chi(\underline{u} - \underline{u}_s) \, dV + \frac{d}{dt} \int_{\Omega_s} \underline{u}_s \, dV$$

$$(2.10) \quad \underline{m} = \oint_{\partial\Omega_s} \underline{r} \times (\sigma \cdot \underline{n}) \, d\gamma = \frac{1}{C_\eta} \int_{\Omega} \underline{r} \times \chi(\underline{u} - \underline{u}_s) \, dV + \frac{d}{dt} \int_{\Omega_s} \underline{r} \times \underline{u}_s \, dV,$$

where the additional terms are denoted ‘unsteady corrections’, as pointed out in [45].

Based on the physical interpretation of C_η as permeability, it is intuitively clear that C_η must be set small enough for the penalization method to yield reasonable results which is reflected by the convergence rate of $\mathcal{O}(\sqrt{C_\eta})$. However, the choice of C_η is subject to constraints, as the penalized equations are discretized and solved numerically. The modeling error of order $\mathcal{O}(\sqrt{C_\eta})$ should be of the same order as the discretization error [32]. It is first noted that in eqn. (2.5), C_η has the dimension of a time. It is instructive to put the nonlinear, viscous and pressure terms aside for a moment. One is then left with $\partial_t u = -u/C_\eta$ inside the solid, with the obvious solution $u = u_0 \exp(-t/C_\eta)$. Thus, C_η can be directly identified as the relaxation time. Interfering with the time step Δt , usually implying $\Delta t/C_\eta < \text{const}$, where const is determined by the stability of the time integration scheme. This simple fact has important consequences for the numerical solution. It indicates that a good choice for C_η is not only “small enough”, but also “as large as possible”. Further insight in the properties of the penalization method can be obtained considering the penalization boundary layer of width $\delta_\eta = \sqrt{\nu C_\eta}$, which forms inside the obstacle Ω_s , as shown in [7]. When increasing the resolution, the number of points per boundary layer thickness, $K = \delta_\eta/\Delta x$, should be kept constant, which implies the relation $C_\eta \propto (\Delta x)^2$, consistent with [32], where the penalized Laplace and Stokes operators were analyzed analytically and numerically. With the scaling for C_η , one still has to choose the constant K . In fact, for any value of K , the method will converge with the same convergence rate, but the error offset can be tuned. For the two-dimensional Couette flow, in [11] we reported the optimal value of $K = 0.128$. In a range of numerical validation tests, including the ones presented here, we find $K = 0.1 - 0.4$ as a good choice which we recommend as a guideline for practical applications.

2.2. Penalization method for moving boundary problems. The volume penalization method as discussed so far assumes a discontinuous mask function in the form of eqn. (2.8). When applying the method to a non-grid aligned body, for example a circular cylinder, the mask function geometrically approximates the boundary to first order in Δx . Results for stationary cylinder using the discontinuous mask function are acceptable [39, 41], but spurious oscillations in the case of moving ones are reported [22]. The reason is that the discontinuous mask can be translated only by integer multiples of the grid spacing, and this jerky motion causes large oscillations in the aerodynamic forces. Kolomenskiy and Schneider [22] proposed an algorithm to shift the mask function in Fourier space instead of physical space. In the present work, we employ a different approach, because displacing the mask in Fourier space involves (additional) Fourier transforms, which are computationally expensive, especially if more than one rigid body is considered, as it is the case here. The idea on hand is to directly assume the mask function to be smoothed over a thin smoothing layer [9, 11]. To this end, we introduce the signed distance function $\delta(\underline{x}, t)$ [33], and

the mask function can then be computed from the signed distance, using

$$(2.11) \quad \chi(\delta) = \begin{cases} 1 & \delta \leq -h \\ \frac{1}{2} (1 + \cos(\pi \frac{\delta+h}{2h})) & -h < \delta < +h \\ 0 & \delta > +h \end{cases}$$

where the semi-thickness of the smoothing layer, h , is used. It is typically defined relative to the grid size, $h = C_{\text{smth}} \Delta x$, thus eqn. (2.11) converges to a Heaviside step function as $\Delta x \rightarrow 0$. Nonetheless, it can be translated by less than one grid point, and then be resampled on the Eulerian fluid grid.

2.3. Wake removal techniques. The penalized Navier–Stokes equations (2.5–2.7) do, by principle, not require boundary conditions on $\partial\Omega_s$ and furthermore we intend to discretize them in a periodic domain Ω . In such a periodic setting, the wake re-enters the domain, which is an undesired artifact. To overcome it, a supplementary “sponge” penalization term can be added to the vorticity-velocity formulation of the Navier–Stokes equations, in order to gradually damp the vorticity [9, 11]. The sponge penalization parameter C_{sp} is usually set to a larger value than C_η , typically $C_{\text{sp}} = 10^{-1}$. The larger value and its longer relaxation time ensure that if a traveling vortex pair enters the sponge region, the leading one is not dissipated too fast, because it otherwise could leave the partner orphaned in the domain. Applying the Biot–Savart operator to the vorticity-velocity formulation we formally find $-\frac{1}{C_{\text{sp}}} \nabla \times \frac{(\chi_{\text{sp}} \omega)}{\nabla^2}$, and thus we have

$$(2.12) \quad \partial_t \underline{u} + \underline{\omega} \times \underline{u} = -\nabla \Pi + \nu \nabla^2 \underline{u} - \frac{\chi}{C_\eta} (\underline{u} - \underline{u}_s) - \frac{1}{C_{\text{sp}}} \nabla \times \frac{(\chi_{\text{sp}} \omega)}{\nabla^2}.$$

Since $\nabla \cdot \underline{u} = 0$, \underline{u} takes the form $\underline{u} = \nabla \times \underline{\psi}$ and the vorticity is $\omega = \nabla \times \underline{u} = \nabla \times \nabla \times \underline{\psi} = -\nabla^2 \underline{\psi}$. Thus for each component ψ_i of the streamfunction $\underline{\psi}$, we solve a Poisson equation, $\nabla^2 \psi_i = \omega_i$, and afterwards, the curl of the streamfunction yields the velocity. By construction the sponge term is divergence-free, which is important since otherwise it would contribute to the pressure, which in turn would be modified even in regions far away from the sponge due to its nonlocality. Moreover, it leaves the mean flow, i.e., the zeroth Fourier mode, unchanged. This technique is well adapted to spectral discretizations, since computing the sponge term requires the solution of three Poisson problems, which becomes a simple division in Fourier space.

Dirichlet conditions on the velocity can be imposed directly with the volume penalization, which applies for example to channel walls. For simulations in a uniform, unbounded free-stream, we use both techniques; in a small layer at the domain borders, the Dirichlet condition $\underline{u} = \underline{u}_\infty$ is imposed with the same precision as the actual obstacle, and a preceding, thicker sponge layer ensures that the upstream influence is minimized [11]. The sponge technique is similar to the “fringe regions” proposed by Schlatter et al. [38]. However, [38] used a velocity sponge only, which lacks the favorable properties of the vorticity sponge described here.

2.4. Discretization. The model equations (2.12) described above can be discretized with any numerical scheme, in particular a Fourier pseudospectral discretization can be used [39, 22, 11]. The general idea is to represent field variables as truncated Fourier series, thus in three dimensions we have for any quantity q (velocity, pressure, vorticity)

$$q(\underline{x}, t) = \sum_{k_x=0}^{N_x-1} \sum_{k_y=0}^{N_y-1} \sum_{k_z=0}^{N_z-1} \hat{q}(\underline{k}, t) \exp(i \underline{k} \cdot \underline{x}) \quad \underline{x} \in [0, 2\pi)^3$$

where $\iota = \sqrt{-1}$ is the complex unit, $\underline{k} = (k_x, k_y, k_z)^T$ is the wavevector and \hat{q} are the discrete complex Fourier coefficients of q . They can be computed efficiently with the fast Fourier transform (FFT) [8]. The gradient of a scalar can for instance be obtained by multiplying the Fourier coefficients with the wavevector and the complex unit, $\widehat{\nabla} q = \iota \underline{k} \hat{q}$. The Laplace operator becomes a simple multiplication by $-|\underline{k}|^2$, and its inversion hence becomes trivial. When using, e.g., finite differences, the dominant part of computational efforts is spent on solving Poisson's equation in every time step [17]. This is a strong motivation to employ a Fourier discretization, as inverting a diagonal operator becomes a simple division. Inserting the truncated Fourier series into the model equations and requiring that the residual vanishes with respect to all test functions (which are identical with the trial functions $\exp(\iota \underline{k} \cdot \underline{x})$) yields a Galerkin projection and results in an evolution equation for the Fourier coefficients of the velocity. The nonlinear and penalization terms contain products, which become convolutions in Fourier space. To facilitate computation, the products are calculated in physical space. This last introduces aliasing errors which are virtually eliminated by the 2/3 rule [6], meaning that only 2/3 of the Fourier coefficients are retained. Such a mixture of spectral and physical computations is generally labeled "pseudo-spectral" and is, when de-aliased, equivalent to a Fourier-Galerkin scheme. Denoting the Fourier transformation with \mathcal{F} , the source terms of eqn. (2.12) read before applying the projection operator

$$(2.13) \quad \hat{\underline{F}}^* = \mathcal{F} \left(-\underline{\omega} \times \underline{u} - \frac{\chi}{C_\eta} (\underline{u} - \underline{u}_s) \right) - \nu |\underline{k}|^2 \hat{\underline{u}} - \frac{1}{C_{sp}} \frac{\iota \underline{k}}{|\underline{k}|^2} \times \mathcal{F}(\chi_{sp} \underline{\omega}),$$

where the diffusive term is only added if no integrating factor technique is used. A Poisson equation for the pressure can be obtained by taking the divergence of eqn. (2.12)

$$(2.14) \quad \nabla^2 \Pi = \nabla \cdot \left(-\underline{\omega} \times \underline{u} - \frac{\chi}{C_\eta} (\underline{u} - \underline{u}_s) \right),$$

and adding the pressure in Fourier space projects the right hand side to the incompressible manifold,

$$\hat{\underline{F}} = \hat{\underline{F}}^* + \iota \underline{k} \left[\frac{\iota \underline{k}}{|\underline{k}|^2} \cdot \hat{\underline{F}}^* \right],$$

which corresponds to a Riesz projector. The spatially discretized equations can then be advanced in time in Fourier space. The choice of time discretization depends on whether the time step Δt is limited by the CFL condition, $\Delta t_u = \text{CFL} \Delta x / u_{max}$, the penalization constant $\Delta t_\eta = D_1 C_\eta$ or the diffusive term $\Delta t_\nu = 0.5 \Delta x^2 / \nu$, since $\Delta t = \min(\Delta t_u, \Delta t_\eta, \Delta t_\nu)$. The constant D_1 depends on the time marching scheme but is of order one. If $\Delta t_u \leq 4 \Delta t_\eta$ and $\Delta t_u \leq 0.5 \Delta x^2 / \nu$, we employ a classical Runge–Kutta method (RK4) with explicit discretization of the diffusion. Otherwise, we use a second order Adams–Bashforth (AB2) scheme with the integrating factor technique that exploits the diagonality of the Laplace operator in Fourier space, and thus treats the diffusion term in an exact fashion [39]. For this scheme, the fully discretized eqn. reads

$$\hat{\underline{u}}^{n+1} = \exp \left(-\nu \Delta t^{n+1} |\underline{k}|^2 \right) \left(\hat{\underline{u}}^n + \beta_{10} \hat{\underline{F}}^n + \beta_{11} \hat{\underline{F}}^{n-1} \exp \left(-\nu \Delta t^n |\underline{k}|^2 \right) \right),$$

where β_{10} and β_{11} are constants depending on the time step. For details we refer to [39]. The AB2 scheme requires only one evaluation of the right hand side, whereas RK4 requires four. The choice of time stepper is thus determined by the computational cost only.

Besides the fast solution of Poisson problems, the spectral method has the advantage of not adding numerical diffusion or dispersion to the discretized penalized equation, unlike it is the case when using finite differences. Furthermore, most of the computational effort is concentrated in the Fourier transforms, which is advantageous from a computational point of view. However, the discretization requires the use of an equidistant grid which implies a large number of grid points.

3. Parallel implementation. The proposed framework is intended to be applicable also for higher Reynolds number flow, for which small spatial and temporal vortical structures appear. To resolve these scales, high resolution and therefore the usage of high-performance computers is required. To this end, our code is designed to compute on massively parallel machines with distributed memory architectures. The parallel implementation is based on the MPI protocol and written in FORTRAN95. The FFTs are computed using the P3DFFT library [34], which provides a parallel data decomposition framework, and FFTW [13], which is used for the one-dimensional Fourier transforms inside P3DFFT. The flow variables are stored on the three-dimensional Cartesian computational grid. Each MPI process only holds a portion of the total data, and the parallel decomposition is performed on at most two indices, i.e., a pencil decomposition is used. The x -direction is not split among processes, the code can thus run on $N_y N_z$ processes at most. This limitation is however not of practical importance, since $N_y N_z$ usually exceeds the number of available CPUs.

The flow chart of the code is illustrated in figure 3.1. All parameters, like the resolution etc., are read from a *.ini file, which avoids recompiling the code every time a parameter is changed. Owing to our numerical approach, the software can be highly modularized. The geometry is entirely contained in the mask function χ and the velocity of the solid \underline{u}_s . Thus the task of adding the actual insect to the spectral fluid solver boils down to constructing χ and \underline{u}_s for a given time t . The following section describes how this is done in detail.

The parallel scaling with the number of CPUs is an important test for numerical codes. Figure 3.1 shows strong scaling tests for a flow resolution of 256^3 and 768^3 grid points and excellent scaling is observed for up to 2048 and 8192 cores, respectively. The reference is the lowest number of cores, since the number of grid points is too large for serial computation on the same machine. For the file input and output for flow field data the hierarchical data format (HDF5) library is employed, in order to guarantee maximum compatibility with third-party applications, such as Matlab and Paraview, the latter is used for the visualizations shown in the results section.

4. Virtual insect model. We previously described the fluid module where the geometry is taken into account by the penalization method, which is the interface with the insect module described next.

Insects fly by flapping their wings. Their wings are basically flat with sharp edges and operate typically at high angle of attack. In the following, we describe the insect framework used in this work in detail, the essential task being to construct χ and \underline{u}_s which enter eqn. (2.12). The virtual insect consists of a body and two wings, all of which are performing solid body rotations around three axes and assumed to be rigid.

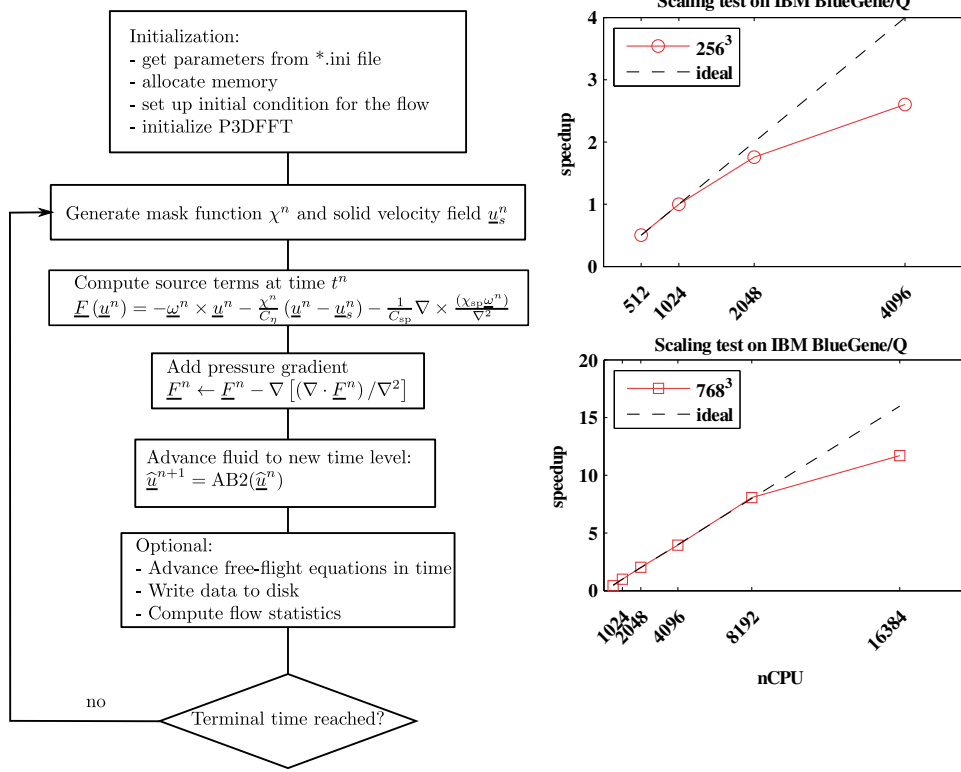


FIGURE 3.1. Left: Flow chart diagram of the numerical code. Right: parallel scaling tests on a large-scale computing cluster of type IBM BlueGene/Q.

Therefore, we will make use of the rotation matrices

$$\begin{aligned}
 R_x(\xi) &= \begin{pmatrix} 1 & 0 & 0 \\ 0 & \cos \xi & \sin \xi \\ 0 & -\sin \xi & \cos \xi \end{pmatrix} & R_y(\xi) &= \begin{pmatrix} \cos \xi & 0 & -\sin \xi \\ 0 & 1 & 0 \\ \sin \xi & 0 & \cos \xi \end{pmatrix} \\
 R_z(\xi) &= \begin{pmatrix} \cos \xi & \sin \xi & 0 \\ -\sin \xi & \cos \xi & 0 \\ 0 & 0 & 1 \end{pmatrix}
 \end{aligned}$$

and define the different reference frames, namely the global $\underline{x}^{(g)}$, body $\underline{x}^{(b)}$, stroke plane $\underline{x}^{(s)}$ and wing $\underline{x}^{(w)}$, in which the geometry is defined. As described above, the mask function is constructed in each evaluation of the right hand side as a function of the signed distance function, $\chi(\underline{x}) = \chi(\delta(\underline{x}))$, according to eqn. (2.11).

4.1. Body system. The insect's body is responsible for a major part of the total drag force. It is described by its logical center $\underline{x}_{\text{cntr}}^{(g)}$, the translational velocity $\underline{u}_{\text{cntr}}^{(g)}$ and the body angles β (pitch), γ (yaw) and ψ (roll), see figure 4.1 The center point $\underline{x}_{\text{cntr}}^{(g)}$ does not necessarily coincide with the center of gravity, it is rather an arbitrary point of reference. A point $\underline{x}^{(g)}$ in the global coordinate system can be transformed to the body system using the following linear transformation

$$\underline{x}^{(b)} = M_{\text{body}}(\psi, \beta, \gamma) \left(\underline{x}^{(g)} - \underline{x}_{\text{cntr}}^{(g)} \right)$$

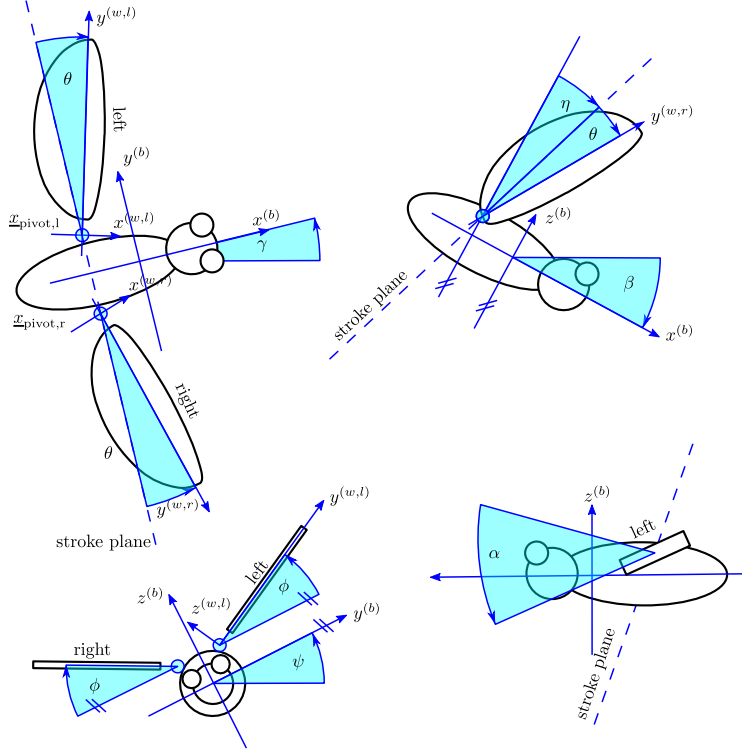


FIGURE 4.1. Model insect with definitions of the body angles γ (yaw), β (pitch), ψ (roll), the anatomical stroke plane angle η , the wing coordinate systems and the wing angles θ (deviation), ϕ (position) and α (feathering). All angles are shown with positive sign.

$$(4.1) \quad M_{\text{body}} = R_x(\psi) R_y(\beta) R_z(\gamma).$$

Since rotation matrices do not commute, it is important to note that the body is first yawed, then pitched and finally rolled, which is conventional in flight mechanics. The geometry of the body is defined in the body reference frame. The angular velocity of the body in the global system is

$$\begin{aligned} \underline{\Omega}_b^{(g)} &= R_z^{-1}(\gamma) \left[\begin{pmatrix} 0 \\ 0 \\ \dot{\gamma} \end{pmatrix} + R_y^{-1}(\beta) \left[\begin{pmatrix} 0 \\ \dot{\beta} \\ 0 \end{pmatrix} + R_x^{-1}(\psi) \begin{pmatrix} \dot{\psi} \\ 0 \\ 0 \end{pmatrix} \right] \right] \\ \underline{\Omega}_b^{(b)} &= M_{\text{body}} \underline{\Omega}_b^{(g)} \end{aligned}$$

which defines the velocity field inside the insect resulting from the body motion,

$$(4.2) \quad \underline{u}_b^{(g)} = \underline{u}_{\text{cntr}}^{(g)} + M_{\text{body}}^{-1} \left(\underline{\Omega}_b^{(b)} \times \underline{x}^{(b)} \right).$$

Equation (4.2) is valid also in the wings, since the flapping motion is prescribed relative to the body.

4.2. Body shape. The body shape is described in the body reference frame described previously. For instance, for the body depicted in figure 4.1, which is composed of an ellipsoidal shaped thorax and spheres for the head and eyes, the

signed distance function is the intersection of the distance functions for the thorax, head and eyes,

$$(4.3) \quad \delta_{\text{body}} = \max(\delta_{\text{thorax}}, \delta_{\text{head}}, \delta_{\text{eyes}}).$$

The max operator of the signed distances in eqn. (4.3) represents the intersection operator [33]. The signed distances for the components read

$$\begin{aligned} \delta_{\text{thorax}}(\underline{x}^{(b)}) &= \sqrt{(y^{(b)})^2 + (z^{(b)})^2} - \sqrt{b^2 \left(1 - (x^{(b)}/a)^2\right)} \\ \delta_{\text{head}}(\underline{x}^{(b)}) &= \left| \underline{x}^{(b)} - \underline{x}_{0,\text{head}}^{(b)} \right| \\ \delta_{\text{eyes}}(\underline{x}^{(b)}) &= \left| \underline{x}^{(b)} - \underline{x}_{0,\text{eyes}}^{(b)} \right|, \end{aligned}$$

where a, b define the axes of the thorax ellipsoid and $\underline{x}_{0,\text{head,eyes}}^{(b)}$ are the centers of the spheres. The body shape in figure 5.3 is obtained by sweeping the radius

$$R(s) = \begin{cases} \max(0, -1.299s^2 + 0.94s + 0.03) & s < 0.6333 & \text{abdomen} \\ \max(0, -2.16s^2 + 3.47s - 1.21) & 0.6333 < s < 1 & \text{thorax} \\ \max(0, -12.68s^2 + 27.49s - 14.73) & 1 < s < 1.2 & \text{head} \end{cases}$$

around an arc-segment of radius $r_{\text{bc}} = 0.95$ centered at $x_{\text{bc}}^{(b)} = -0.245$, $z_{\text{bc}}^{(b)} = -0.93$. Other available options can be found in the source code documentation.

4.3. Wing system. We consider only insects with two wings, one on each side, that are rotating about the pivot points $\underline{x}_{\text{pivot,r}}^{(b)}$ and $\underline{x}_{\text{pivot,l}}^{(b)}$. These pivots do not necessarily lie on the body surface; we rather allow a gap between wings and body. This gap avoids problems with non-solenoidal velocity fields at the wing base. It is conventional to introduce a stroke plane, which is a plane tilted with respect to the body by an angle η . The coordinate in the stroke plane reads

$$\underline{x}^{(s)} = M_{\text{stroke}} \left(\underline{x}^{(b)} - \underline{x}_{\text{pivot}}^{(b)} \right).$$

Here, we use an anatomical stroke angle, that is, the angle η is defined relative to the body. Within the stroke plane, the wing motion is described by the angles α (feathering angle or angle of attack), ϕ (positional or flapping angle), θ (deviation or out-of-stroke angle). Applying two rotation matrices yields the transformation from the body to the wing coordinate system:

$$\underline{x}^{(w)} = M_{\text{wing}} \underline{x}^{(s)} = M_{\text{wing}} M_{\text{stroke}} \left(\underline{x}^{(b)} - \underline{x}_{\text{pivot}}^{(b)} \right).$$

When flapping symmetrically, i.e., both wings following the same motion protocol, the stroke and wing rotation matrices for the left and right wing are given by

$$\begin{aligned} M_{\text{stroke,l}} &= R_y(\eta) & M_{\text{stroke,r}} &= R_x(\pi) R_y(\eta) \\ M_{\text{wing,l}} &= R_y(\alpha) R_z(-\theta) R_x(\phi) & M_{\text{wing,r}} &= R_y(-\alpha) R_z(-\theta) R_x(-\phi) \end{aligned}$$

due to the rotation $R_x(\pi)$ the sign of θ for the right wing does not have to be inverted. The angular velocities of the wings are given by

$$\begin{aligned} \underline{\Omega}_w^{(b)} &= M_{\text{stroke}}^{-1} \left[R_x^{-1}(\phi) \left[\begin{pmatrix} \dot{\phi} \\ 0 \\ 0 \end{pmatrix} + R_z^{-1}(-\theta) \left[\begin{pmatrix} 0 \\ 0 \\ -\dot{\theta} \end{pmatrix} + R_y^{-1}(\alpha) \begin{pmatrix} 0 \\ \dot{\alpha} \\ 0 \end{pmatrix} \right] \right] \right] \\ \underline{\Omega}_w^{(w)} &= M_{\text{wing}} \underline{\Omega}_w^{(b)} \end{aligned}$$

which is used to compute the velocity field resulting from the wing motion,

$$(4.4) \quad \begin{aligned} \underline{u}_w^{(w)} &= \underline{\Omega}_w^{(w)} \times \underline{x}^{(w)} \\ \underline{u}_w^{(g)} &= M_{\text{body}}^{-1} M_{\text{wing}}^{-1} M_{\text{stroke}}^{-1} \underline{u}_w^{(w)}. \end{aligned}$$

The total velocity field inside the wings is given as the superposition of the body and wing rotation,

$$\underline{u}_s^{(g)}(\underline{x} \in \{\underline{x}_w\}) = \underline{u}_w^{(g)} + \underline{u}_b^{(g)}.$$

The actual kinematics, i.e., the angles $\alpha(t)$, $\phi(t)$ and $\theta(t)$ are parametrized by either Fourier or Hermite interpolation coefficients and read from a small text file.

4.4. Wing shape. In the previous section we defined the wing reference frame $\underline{x}^{(w)}$, in which we now describe the wing's signed distance function δ . In general, we define a set of several signed distance functions, each of which describes one surface of the wing. The signed distance function of the entire wing is then given by their intersection. For some model insects, we consider simple wings for which straightforward analytical expressions are available. For a rectangular wing, for instance the one illustrated in figure 5.2 (c), we find for the signed distance function

$$(4.5) \quad \delta(\underline{x}^{(w)}) = \max\left(x^{(w)} - b; x^{(w)} - (B - b); y^{(w)} - 1; a - y^{(w)}; |z| - h/2\right).$$

For realistic insect wings however, we parametrize the wing shape in polar coordinates. As illustrated in figure 4.2, the shape in the wing plane is described by the center point $\underline{x}_c^{(w)}$, which is arbitrary as long as the function $R(\vartheta)$ is unique for all ϑ . To sample the wing on a computational grid, we need a function $R(\vartheta)$ that can be evaluated for all ϑ . As $R(\vartheta)$ is naturally 2π -periodic, a truncated Fourier series can be used:

$$(4.6) \quad R(\vartheta) = \frac{a_0}{2} + \sum_{i=1}^N a_i \cos(2\pi i \vartheta) + \sum_{i=1}^N b_i \sin(2\pi i \vartheta)$$

In practice, eqn (4.6) has to be evaluated for all grid points in the vicinity of the wing, which requires $\mathcal{O}(N_x N_y N_z)$ evaluations with a small constant. The computational cost can however be significant, which is why eqn. (4.6) is evaluated for 25 000 values of ϑ once during initialization. Afterwards, linear interpolation is used for its lower computational cost. The signed distance for such a wing then reads

$$\delta(\underline{x}^{(w)}) = \max\left(\left|z^{(w)}\right| - h/2; r(\vartheta) - R(\vartheta)\right).$$

If a wing cannot be described by one radius, because $R(\vartheta)$ is not unique, several radii and center points can be used [4].

4.5. Power requirement. Actuating the wings requires power expenditures that are very difficult to measure directly. In numerical simulations, the power can be obtained directly, since the aerodynamic torque moment \underline{m} with respect to the wing pivot point is available from eqn. (2.10). The power P_{aero} required to move one wing is found to be

$$(4.7) \quad P_{\text{aero}} = -\underline{m} \cdot (\underline{\Omega}_w - \underline{\Omega}_b)$$

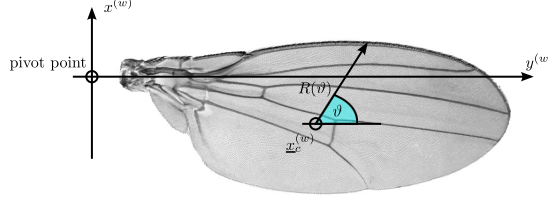


FIGURE 4.2. Realistic wing shapes are described in polar coordinates $R(\vartheta)$.

which is equivalent to the definition $P_{\text{aero}} = \int \underline{u} d\underline{F}$ given in [27]. The power can also be computed directly from the penalization term, $P_{\text{aero}} = \frac{1}{C_\eta} \int_\Omega \underline{u}_s \chi (\underline{u} - \underline{u}_s) dV$. In addition to the aerodynamic power, the inertial power has to be expended, i.e., the power required to move the wing in vacuum. As the flapping motion is periodic, its stroke averaged value is zero. The inertial power P_{inert} is positive if the wing is accelerated (power consumed) and negative if it is decelerated. The definition is

$$P_{\text{inert}} = \underline{\Omega}_w^{(w)} \cdot \left(\underline{J}_w^{(w)} \dot{\underline{\Omega}}_w^{(w)} + \underline{\Omega}_w^{(w)} \times \underline{J}_w^{(w)} \underline{\Omega}_w^{(w)} \right)$$

with the wing tensor of inertia $\underline{J}_w^{(w)}$ [3]. The sum of inertial and aerodynamic power can be negative during deceleration phases, which would mean that the insect can store energy in its muscles. It is unknown to what extent this can be realized, and it is thus often conservatively assumed that energy storage is not possible, in which case the total power P_{total} is given by $P_{\text{total}} = \max(P_{\text{inert}} + P_{\text{aero}}, 0)$.

4.6. Governing equations in free flight. Hitherto we have considered the insect to be fixed, i.e., tethered in the computational domain. In free flight, additional equations have to be solved together with the fluid, namely Newton's law. The body translation is then governed by

$$M \dot{\underline{u}}_{\text{centr}}^{(g)} = \underline{F}^{(g)}$$

where $\underline{F}^{(g)}$ contains the aerodynamic and gravitational forces and M is the mass of the insect. For simplicity, $\underline{x}_{\text{centr}}$ and $\underline{u}_{\text{centr}}$ correspond to the center of gravity in the case of free flight. To handle the rotational degrees of freedom, we employ a quaternion based formulation, similar to the one proposed in [26], which avoids the 'Gimbal lock' problem. The governing equation for the angular velocity $\underline{\Omega}^{(b)}$ in the body reference frame reads

$$\underline{J}^{(b)} \dot{\underline{\Omega}}^{(b)} + \begin{pmatrix} 0 & -\Omega_z^{(b)} & \Omega_y^{(b)} \\ \Omega_z^{(b)} & 0 & -\Omega_x^{(b)} \\ -\Omega_y^{(b)} & \Omega_x^{(b)} & 0 \end{pmatrix} \underline{J}^{(b)} \underline{\Omega}^{(b)} = \underline{m}^{(b)},$$

where $\underline{J}^{(b)}$ is the moment of inertia around the body axes $(x^{(b)}, y^{(b)}, z^{(b)})$ and \underline{m} is the vector of torque moments as defined in eqn. (2.10). The skew-symmetric term stems from the change into a moving reference frame. We introduce the normalized quaternion ε with components ε_i , $i = 0, \dots, 3$, $\sum \varepsilon_i^2 = 1$. The governing equations for the quaternion state are

$$\dot{\varepsilon} = \frac{1}{2} \underline{S}^T \underline{\Omega}^{(b)}$$

with the matrix

$$S = \begin{pmatrix} -\varepsilon_1 & \varepsilon_0 & \varepsilon_3 & -\varepsilon_2 \\ -\varepsilon_2 & -\varepsilon_3 & \varepsilon_0 & \varepsilon_1 \\ -\varepsilon_3 & \varepsilon_2 & -\varepsilon_1 & \varepsilon_0 \end{pmatrix}.$$

Assuming $\underline{\underline{J}}^{(b)}$ to be constant the body axes to be the principal axes of inertia (i.e., $\underline{\underline{J}}^{(b)}$ is diagonal), the following first order system set of 13 equations is obtained

$$(4.8) \quad \frac{d}{dt} \begin{pmatrix} x_{\text{cntr}}^{(g)} \\ y_{\text{cntr}}^{(g)} \\ z_{\text{cntr}}^{(g)} \\ u_{\text{cntr},x}^{(g)} \\ u_{\text{cntr},y}^{(g)} \\ u_{\text{cntr},z}^{(g)} \\ \varepsilon_0 \\ \varepsilon_1 \\ \varepsilon_2 \\ \varepsilon_3 \\ \Omega_x^{(b)} \\ \Omega_y^{(b)} \\ \Omega_z^{(b)} \end{pmatrix} = \frac{1}{2} \begin{pmatrix} 2u_{\text{cntr},x}^{(g)} \\ 2u_{\text{cntr},y}^{(g)} \\ 2u_{\text{cntr},z}^{(g)} \\ 2F_x^{(g)}/M \\ 2F_y^{(g)}/M \\ 2(F_z^{(g)}/M - g) \\ -\varepsilon_1\Omega_x^{(b)} - \varepsilon_2\Omega_y^{(b)} - \varepsilon_3\Omega_z^{(b)} \\ \varepsilon_0\Omega_x^{(b)} - \varepsilon_3\Omega_y^{(b)} + \varepsilon_2\Omega_z^{(b)} \\ \varepsilon_3\Omega_x^{(b)} + \varepsilon_0\Omega_y^{(b)} - \varepsilon_1\Omega_z^{(b)} \\ -\varepsilon_2\Omega_x^{(b)} + \varepsilon_1\Omega_y^{(b)} + \varepsilon_0\Omega_z^{(b)} \\ \left((J_y^{(b)} - J_z^{(b)}) \Omega_y^{(b)} \Omega_z^{(b)} + m_x^{(b)} \right) / J_x^{(b)} \\ \left((J_z^{(b)} - J_x^{(b)}) \Omega_z^{(b)} \Omega_x^{(b)} + m_y^{(b)} \right) / J_y^{(b)} \\ \left((J_x^{(b)} - J_y^{(b)}) \Omega_x^{(b)} \Omega_y^{(b)} + m_z^{(b)} \right) / J_z^{(b)} \end{pmatrix}$$

which is solved with the same time discretization as the fluid. The rotation matrix M_{body} is then computed from the quaternion ε_i

$$(4.9) \quad M_{\text{body}} = \begin{pmatrix} \varepsilon_0^2 + \varepsilon_1^2 - \varepsilon_2^2 - \varepsilon_3^2 & 2(\varepsilon_1\varepsilon_2 - \varepsilon_3\varepsilon_0) & 2(\varepsilon_1\varepsilon_3 + \varepsilon_2\varepsilon_0) \\ 2(\varepsilon_1\varepsilon_2 + \varepsilon_3\varepsilon_0) & \varepsilon_0^2 - \varepsilon_1^2 + \varepsilon_2^2 - \varepsilon_3^2 & 2(\varepsilon_2\varepsilon_3 - \varepsilon_1\varepsilon_0) \\ 2(\varepsilon_1\varepsilon_3 - \varepsilon_2\varepsilon_0) & 2(\varepsilon_2\varepsilon_3 + \varepsilon_1\varepsilon_0) & \varepsilon_0^2 - \varepsilon_1^2 - \varepsilon_2^2 + \varepsilon_3^2 \end{pmatrix},$$

which replaces the definition in eqn. (4.1) in the free-flight case. The initial values at time $t = 0$ for ε_i can conveniently be computed from a set of yaw, pitch and roll angles,

$$\begin{pmatrix} \varepsilon_0 \\ \varepsilon_1 \\ \varepsilon_2 \\ \varepsilon_3 \end{pmatrix} = \begin{pmatrix} \cos(\psi/2) \cos(\beta/2) \cos(\gamma/2) + \sin(\psi/2) \sin(\beta/2) \sin(\gamma/2) \\ \sin(\psi/2) \cos(\beta/2) \cos(\gamma/2) - \cos(\psi/2) \sin(\beta/2) \sin(\gamma/2) \\ \cos(\psi/2) \sin(\beta/2) \cos(\gamma/2) + \sin(\psi/2) \cos(\beta/2) \sin(\gamma/2) \\ \cos(\psi/2) \cos(\beta/2) \sin(\gamma/2) - \sin(\psi/2) \sin(\beta/2) \cos(\gamma/2) \end{pmatrix}.$$

In the actual implementation, we multiply the right hand side of equation (4.8) with a six component vector with zeros or ones, to deactivate some degrees of freedom.

5. Validation. For code validation we consider three test cases, a falling sphere, a rectangular flapping wing and hovering flight of a fruit fly.

5.1. Falling sphere. The first test case to validate the flow solver is the sedimentation of a sphere, which in our terminology is an insect without wings and with a spherical body. We consider case 1 proposed by Mordant and Pinton [31], who studied

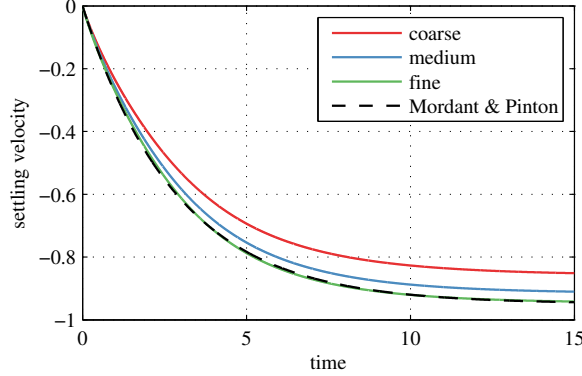


FIGURE 5.1. *Settling velocity of a falling sphere, experimental results by Mordant & Pinton [31] and present results for coarse, medium and fine grids.*

the sedimentation problem experimentally in a water tank. The sphere of unit diameter and mass $M = 1.3404$ is falling in fluid of viscosity $\nu = 0.0228$ and unit density. The dimensionless gravity is $g = 0.8036$ and the terminal settling velocity obtained from the experiments is $U = 0.9488$. We perform a grid convergence test using the domain size $8 \times 8 \times 16$, and parameters $N_x \times N_y \times N_z \times C_\eta$ of a coarse ($96 \times 96 \times 192 \times 10^{-3}$), medium ($192 \times 192 \times 384 \times 2.5 \cdot 10^{-4}$) and fine ($384 \times 384 \times 768 \times 6.25 \cdot 10^{-5}$) grid. The number of points per penalization boundary layer is $K = 0.0573$. The results of the convergence study are illustrated in figure 5.1 and the settling velocity for the finest resolution differs from the experimental findings by less than 1%. The finest resolution required 30 GB of memory and 34 400 CPU hours on 1024 cores to perform 266 667 time steps. The computational cost is relatively high, since small values of C_η are required as the Reynolds number is small.

5.2. Validation case of a rectangular flapping wing. We consider the setup proposed by Suzuki and co-workers in [43] Appendix B2. It considers only one rectangular wing with a finite thickness, neglecting thus the body and the second wing. The fact that the thickness is finite and the geometry rather simple, compared to actual insects, motivates the choice of this setup. The wing kinematics are given by $\phi = \phi_m \cos(2\pi t)$, $\alpha = \frac{\alpha_m}{\tanh c_\alpha} \tanh(c_\alpha \sin(2\pi t))$ and $\theta = 0$, where $\phi_m = 80^\circ$, $\alpha_m = 45^\circ$, $c_\alpha = 3.3$; the motion is symmetric for the up- and downstroke and depicted in figure 5.2 (a-b). The rectangular wing and the wing coordinate system are illustrated in figure 5.2 (c). We normalize the distance from pivot to tip to unity, which yields $a = 1.6667$, $b = 0.0667$, $B = 0.4167$ and a wing thickness of $h = 0.04171$. The Reynolds number is set to $\text{Re} = U_{\text{tip}} B / \nu = 100$ with $U_{\text{tip}} = 2\pi\phi_m$, yielding the kinematic viscosity $\nu = 0.0366$. In the present simulations, we discretize the domain of size $3 \times 3 \times 3$ using $512 \times 512 \times 512$ points and a penalization parameter of $C_\eta = 1.25 \cdot 10^{-4}$ ($K = 0.365$). The reference computation in [43] is performed in a domain of size $4.16 \times 4.16 \times 4.16$, using a fine grid near the wing and a coarse one in the far-field. Based on the resolution of the fine grid, $\Delta x = B/50$, the corresponding equidistant resolution would be 500^3 . In our simulations, the body reference point is located at $\underline{x}_{\text{cntr}}^{(g)} = (1.5, 1.5, 1.7)$ and coincides with the wing pivot point, thus $\underline{x}_{\text{pivot}}^{(b)} = 0$. The orientation of the body coordinate system is given by $\psi = 0^\circ$, $\beta = -45^\circ$, $\gamma = 45^\circ$ and $\eta = -45^\circ$, where the 45° yaw angle was added to keep the wing as far away from

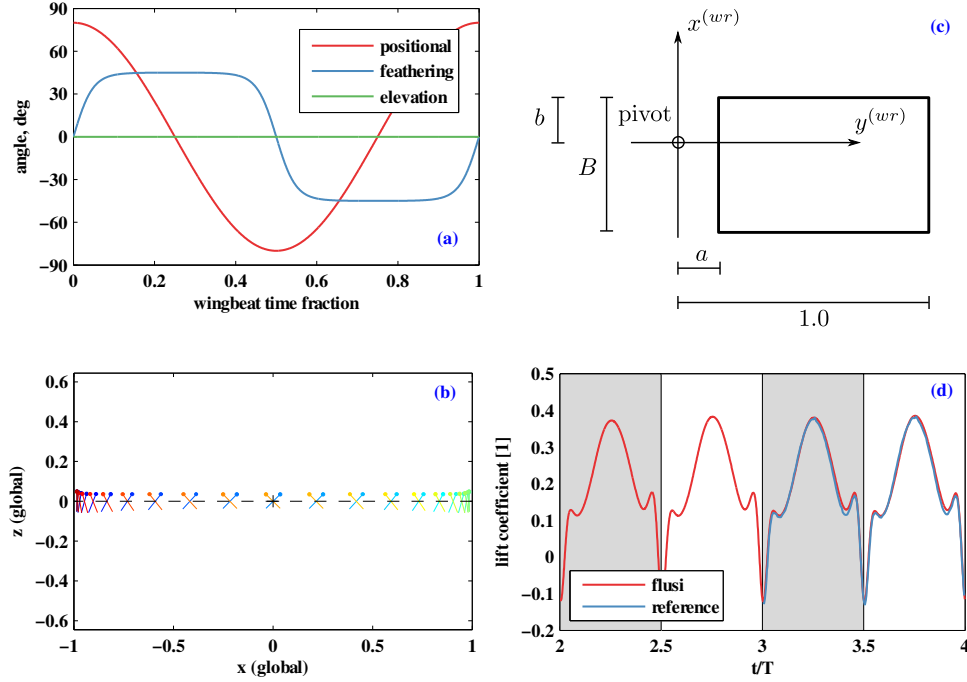


FIGURE 5.2. *Flapping rectangular wing. (a) kinematics used in the test case, as given by Suzuki et al. [43]. (b) visualization of the wing kinematics by a chord section (without body, color represents time) (c) Geometry of the flapping rectangular wing. Contrary to [43], we normalize the distance pivot-wing tip to unity. (d) time evolution of the vertical force acting on the wing for the last two strokes, with the reference solution presented in [43].*

the vorticity sponges as possible. A total of four strokes has been computed, starting with a quiescent initial condition, $\underline{u}(\underline{x}, t = 0) = 0$. The outer boundary conditions on the domain are homogeneous Dirichlet conditions in z -direction and a vorticity sponge, extending over 32 grid points with $C_{sp} = 10^{-1}$, in the remaining ones. The simulation required 35 GB of memory and 5785 CPU hours on 1024 cores. A total of 27 701 time steps was performed.

The resulting time series of the vertical force is illustrated in figure 5.2 (d). It takes the first two wingbeats to develop a periodic state, since the motion is impulsively started, and then the following strokes are almost identical. The present solution agrees well with the reference solution, and the relative R.M.S difference is $\|F - F_{ref}\|_2 / \|F_{ref}\|_2 \approx 4\%$ over the last two periods.

5.3. Hovering flight of a fruit fly model. The third validation test compares with a hovering fruit fly model, of which numerical simulations have been presented by Maeda and Liu [27]. Their simulations are based on overset grids, i.e., a body-fitted grid for the wings ($65 \times 65 \times 11$ each) and the body ($61 \times 61 \times 9$), as well as a background grid ($161 \times 141 \times 127$) have been used to solve the incompressible Navier–Stokes equations, approximated in the artificial compressibility formulation, using a finite volume discretization.

The fruit fly considered is defined in figure 5.3. The wing length from pivot point to wing tip, $R = 2.47$ mm, the fluid density $\rho_f = 1.225$ kg/m³ and the wingbeat frequency $f = 218$ Hz are used for normalization. The body, depicted in figure 5.3

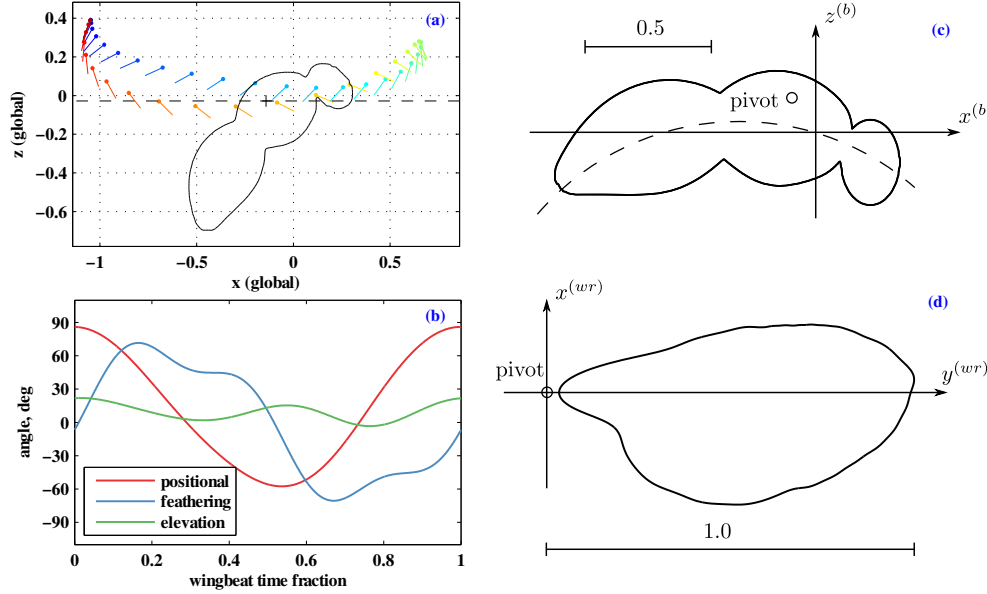


FIGURE 5.3. Hovering fruit fly, for comparison with [27]. (a): wingbeat kinematics in the side view. (b) time evolution of the wing angles. (c) Drawing of the insect's body in the plane $y^{(b)} = 0$. The body is rotationally symmetric with a circular center line. (d) Drawing of the wing shape, together with its pivot point.

(a,c), has an elliptical cross-section with center points following an arched centerline of radius $r_{bc} = 0.94644$ centered at $x_{bc}^{(b)} = -0.244769$, $z_{bc}^{(b)} = -0.9301256$. The wing pivot points are located at $\underline{x}_{\text{pivot,rl}}^{(b)} = (-0.12, \pm 0.1445, 0.08)$. The insect is tethered at $\underline{x}_c^{(g)} = (1.6, 1.6, 1.9)$ in a computational domain of size $3.2 \times 3.2 \times 3.2$, discretized with $640 \times 640 \times 640$ Fourier modes and a penalization parameter of $C_\eta = 1.15 \cdot 10^{-4}$ ($K = 0.23$). Its body orientation is given by $\psi = 0$, $\beta = -45^\circ$, $\gamma = 45^\circ$ and $\eta = -45^\circ$. The fruit fly hovers, thus the body position and orientation do not change in time. A total of four wing beats has been computed, and the initial condition is fluid at rest, $\underline{u}(\underline{x}, t = 0) = \underline{0}$. We apply a vorticity sponge in the x and y -direction (32 grid points thick with $C_{sp} = 10^{-1}$) and impose no-slip boundary conditions in the z -direction, i.e., we impose floor and ceiling. The simulation required 68 GB of memory and 15 100 CPU hours on 1024 cores. A total of 48 200 time steps was performed.

The wing shape is illustrated in figure 5.3 (d). It has a mean chord $c_m = A/R = 0.33$, which yields with the kinematic viscosity of air, $\nu = 1.5 \cdot 10^{-5} \text{ m}^2/\text{s}$ the Reynolds number

$$\text{Re} = \frac{U_{\text{tip}} c_m}{\nu} = \frac{2\Phi R f c_m}{\nu} = 136$$

where $\Phi = 2.44 \text{ rad}$ is the stroke amplitude of the positional angle. The time evolution of the wing kinematics is illustrated in figure 5.3 (b). The up- and downstroke are not symmetric, and the wing trajectory, figure 5.3 (a), shows the characteristic U-shape.

The results for the lift force, normalized with the weight, and the aerodynamic power in W/kg body mass are presented in figure 5.4. As the mass of the model insect was not given in [27], we assumed the fourth stroke of the reference data to balance the weight, yielding $m = 1.02 \text{ mg}$. Small circles at mid-stroke indicate stroke-

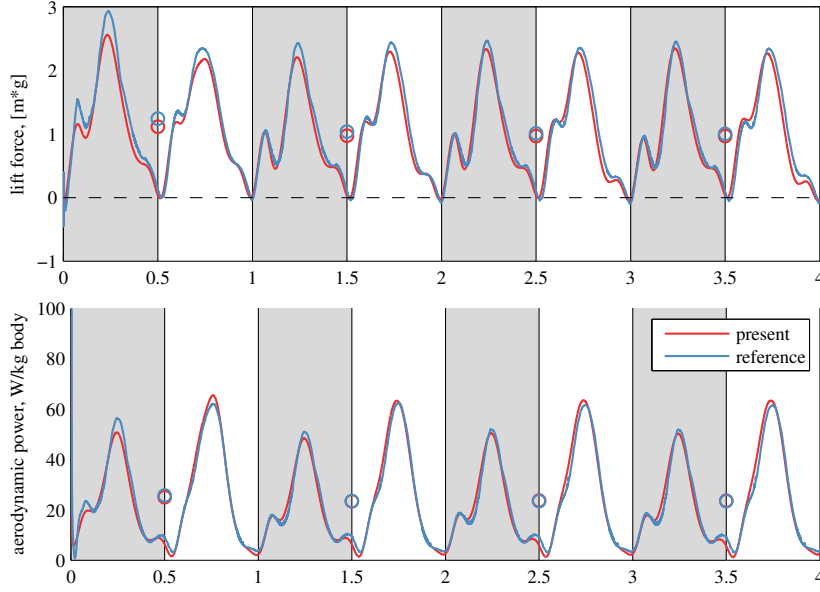


FIGURE 5.4. *Hovering fruit fly, comparison with [27]. Top: total vertical force. Bottom: aerodynamic power. Gray shaded areas denote upstrokes, stroke averages are indicated by circles. The mean values during the last stroke differ by 3.26% and 1.00% for the vertical force and the power, respectively.*

averaged values. For the stroke-averaged vertical force, we find respectively 10.03%, 6.19%, 4.03% and 3.26% relative difference to the reference data for the four strokes computed, which can be explained by the impulsively started motion at the beginning of the first stroke. The time evolution, e.g., the occurrence of peaks, are very similar in both data sets. The agreement is even better for the aerodynamic power, with relative differences of 0.57%, 0.06%, -0.95% and -1.00% for the stroke-averaged values. Both power and lift peak during the translation phase of the up- and downstroke, and reach a minimum value at the reversals.

The flow field generated by the fruit fly model is visualized in figure 5.5 by iso-surfaces of the Q -criterion, for two time instants during the downstroke. For incompressible flows, the Q -criterion can be computed as $Q = \nabla^2 p / 2$, see [23, p. 23].

The first snapshot at $t/T = 0.2$ corresponds to the early downstroke, when the maximum angle of attack (cf. figure 5.3 (b)) is reached, i.e., it is at the beginning of the translation phase. The leading edge vortex on both wings is already formed, and the lift production is close to its peak (cf. figure 5.4). A vortex ring can be observed at the left wing, connecting the wing root and tip. It is formed when the wing begins to change direction at the stroke reversal and therefore termed starting vortex. The tip vortex, however, is continuously formed throughout the stroke, as can be seen in the second snapshot at $t/T = 0.4$, which is shortly before stroke reversal. It is transported downwards by the fluid flow, since the vertical force production requires accelerating fluid momentum in that direction. The first snapshot shows the tip vortex shed during the previous upstroke, which is at that time still connected. In the second snapshot, it is already largely dissipated by the fluid viscosity and no longer a coherent tube. The leading edge vortex can also be observed at $t/T = 0.4$, illustrating that it indeed remains stably attached throughout the stroke.

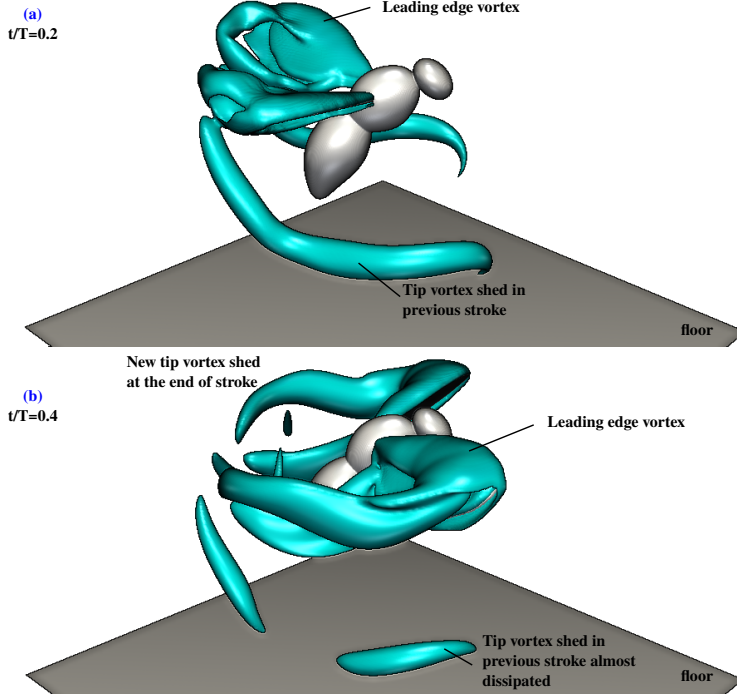


FIGURE 5.5. Snapshot of the vortical structures generated by a hovering fruit fly model, visualized by iso-surfaces of the Q -criterion ($Q = 100$), at two different times of the downstroke (a) at the beginning of the downstroke $t/T = 0.2$ and (b) shortly before the ventral stroke reversal $t/T = 0.4$. The leading edge vortex is formed at the beginning of the downstroke, and at $t/T = 0.2$ is already visible, and remains stably attached until the ventral stroke reversal. The tip vortex shed in the previous upstroke is visible in (a) and almost dissipated in (b).

6. Hovering insect in the turbulent regime. In the previous section we discussed the hovering flight of a fruit fly model. Here the aim is to run the code in the turbulent regime and thus we compute the same model for larger Reynolds number, i.e., at $Re = 1000$, and reduce the viscosity correspondingly to $\nu = 1.16 \cdot 10^{-3}$. All other physical parameters, like the kinematics, are the same as in the previous section. The computational domain is $4 \times 4 \times 6$, resolved with $768 \times 768 \times 1152$ grid points, and the penalization parameter is $C_\eta = 2.5 \cdot 10^{-4}$ ($K = 0.1034$). The simulation requires 175 GB memory and 51 507 CPU hours and was run on 4096 cores. A total of 63698 time steps was performed.

At this Reynolds number, the tip vortices are no longer stable and create a turbulent wake instead. Figure 6.1 shows the wake structure by mean of the Q -criterion (isosurface $Q = 1000$).

7. Conclusions and Perspectives. We presented the versatile open source software FluSI for the numerical simulation of the aerodynamics of flapping insect flight running on massive parallel computer architectures. Different benchmarks demonstrated the efficiency of the code and showed its validity in comparison with results from the literature. A computation of a flapping flight in the turbulent flow regime illustrated the potential of the approach.

The numerical method is based on a Fourier pseudo-spectral discretization of the three-dimensional incompressible Navier–Stokes equations. Thus no artificial numer-

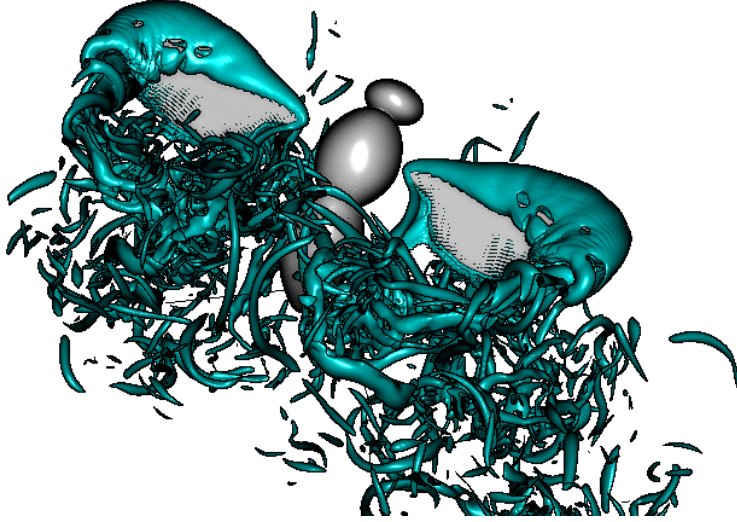


FIGURE 6.1. *Insect model in hovering flight at $Re = 1000$, exhibiting a turbulent wake. Shown is an isosurface of the Q -criterion ($Q = 1000$) at $t/4 = 0.3$. The leading edge vortex is still intact.*

ical diffusion or dispersion are introduced in the discretization. The no-slip boundary conditions for the complexly shaped and time varying geometry of the flapping wings and the insect body are imposed with the volume penalization method. The penalization parameter is chosen such that the modeling error, due to penalization, and the discretization error are balanced. The computational cost of the flow solver is essentially due to the Fourier transforms. Benefiting from the efficient implementation of three-dimensional FFTs, excellent scaling on large scale computing clusters has thus been obtained. A limitation of the current approach is that equidistant Cartesian grids are required and a compromise between the domain size and the number of grid points has to be imposed. The modular structure of the FluSI code permits to design different and complex geometries of the insect shape and its wings easily and also to change their kinematics. For the free flight option, equations in a quaternion-based formulation are solved. Different flow configurations, like channel flows with laminar or turbulent inflow or including bluff bodies of almost arbitrary shape, are possible using penalization together with a sponge technique. For example the forward flight of a bumblebee in a wind tunnel with fully developed turbulent inflow has been computed recently and the aerodynamic forces and flow structures have been studied [12]. Numerical simulations of the ground effect of a fruit fly have also been performed and the aerodynamics has been analyzed [21]. Moreover, in principle the number of insects is not limited to one, only the available computational resources will impose a restriction.

In the current implementation the wings are considered to be rigid, however one-dimensional flexibility, either chordwise or spanwise solving the nonlinear beam equation is already implemented in a fluid-structure module. First tests for 1d flexible flapping foils are promising [10] and for two-dimensional flow configurations extensive benchmarking has already been performed [11]. The latter model has also been applied to insect flight [20]. The extension to two-dimensional flexible wings is a nearby perspective using in a first step a discrete spring model.

REFERENCES

- [1] P. ANGOT, C. BRUNEAU, AND P. FABRIE, *A penalization method to take into account obstacles in incompressible viscous flows*, Numer. Math., 81 (1999), pp. 497–520.
- [2] E. ARQUIS AND J.-P. CALTAGIRONE, *Sur les conditions hydrodynamiques au voisinage d’une interface milieu fluide milieu poreux: application à la convection naturelle*, C. R. Acad. Sci. Paris, Sér. II, 299 (1984).
- [3] G. J. BERMAN AND Z. J. WANG, *Energy-minimizing kinematics in hovering insect flight*, J. Fluid Mech., 582 (2007), pp. 153–168.
- [4] G. BIMBARD, D. KOLOMENSKIY, O. BOUTELEUX, J. CASAS, AND R. GODOY-DIANA, *Force balance in the take-off of a pierid butterfly: relative importance and timing of leg impulsion and aerodynamic forces*, J. Exp. Biol., 216 (2013), pp. 3551–3563.
- [5] O. BOIRON, G. CHIAVASSA, AND R. DONAT, *A high-resolution penalization method for large mach number flows in the presence of obstacles*, Computers & Fluids, 38 (2009), pp. 703–714.
- [6] C. CANUTO, M. Y. HUSSAINI, A. QUARTERONI, AND T. ZANG, *Spectral Methods in Fluid Dynamics*, Springer Verlag, 1986.
- [7] G. CARBOU AND P. FABRIE, *Boundary layer for a penalization method for viscous incompressible flow*, Adv. Diff. Equ., 8 (2003), pp. 1453–2480.
- [8] J. W. COOLEY AND J. W. TUKEY, *An algorithm for the machine calculation of complex Fourier series*, Math. Comput., 19 (1965), pp. 297–301.
- [9] T. ENGELS, D. KOLOMENSKIY, K. SCHNEIDER, AND J. SESTERHENN, *Two-dimensional simulation of the fluttering instability using a pseudospectral method with volume penalization*, Computers & Structures, 122 (2012), pp. 101–112.
- [10] T. ENGELS, D. KOLOMENSKIY, K. SCHNEIDER, AND J. SESTERHENN, *A numerical study of vortex-induced drag of elastic swimmer models*, in Proceedings 6th International Symposium on Aero-aqua Bio-Mechanisms, November 13.-16., Honolulu, Hawaii, USA., 2014.
- [11] T. ENGELS, D. KOLOMENSKIY, K. SCHNEIDER, AND J. SESTERHENN, *Numerical simulation of fluid-structure interaction with the volume penalization method*, J. Comput. Phys., 281 (2015), pp. 96–115.
- [12] T. ENGELS, D. KOLOMENSKIY, K. SCHNEIDER, J. SESTERHENN, AND F.-O. LEHMANN, *Turbulence insignificantly alters mean aerodynamic forces and flight power in bumblebees*, preprint, (6/2015).
- [13] M. FRIGO AND S. G. JOHNSON, *The design and implementation of FFTW3*, Proc. IEEE, 94 (2005), pp. 216–231.
- [14] M. GAZZOLA, W. M. V. REES, AND P. KOUMOUTSAKOS, *C-start: optimal start of larval fish*, J. Fluid Mech., (2012), pp. 1–14.
- [15] M. HEJLESEN, P. KOUMOUTSAKOS, A. LEONARD, AND J. WALTHER, *Iterative Brinkman penalization for remeshed vortex methods.*, J. Comput. Phys., 280 (2015), pp. 547–562.
- [16] C. INTROINI, M. BELLARD, AND C. FOURNIER, *A second order penalized direct forcing for hybrid Cartesian/immersed boundary flow simulations*, Computers & Fluids, 90 (2014), pp. 21–41.
- [17] C. JI, A. MUNJIZA, AND J. WILLIAMS, *A novel iterative direct-forcing immersed boundary method and its finite volume applications*, J. Comput. Phys., 231 (2012), pp. 1797–1821.
- [18] B. KADOCH, D. KOLOMENSKIY, P. ANGOT, AND K. SCHNEIDER, *A volume penalization method for incompressible flows and scalar advection-diffusion with moving obstacles*, J. Comput. Phys., 231 (2012), pp. 4365–4383.
- [19] J. KIM AND P. MOIN, *Application of a fractional-step method to incompressible navier-stokes equations*, J. Comput. Phys., 59 (1985), pp. 308–323.
- [20] D. KOLOMENSKIY, T. ENGELS, AND K. SCHNEIDER, *Numerical modelling of flexible heaving foils*, J. Aero Aqua Bio-mechanisms, 3 (2013), pp. 22–28.
- [21] D. KOLOMENSKIY, M. MAEDA, T. ENGELS, H. LIU, K. SCHNEIDER, AND J.-C. NAVE, *Aero-dynamic ground effect in fruitfly sized insect takeoff*, arXiv preprint arXiv:1504.04484, (2015).
- [22] D. KOLOMENSKIY AND K. SCHNEIDER, *A Fourier spectral method for the Navier-Stokes equations with volume penalization for moving solid obstacles*, J. Comput. Phys., 228 (2009), pp. 5687–5709.
- [23] M. LESIEUR, O. MÉTAIS, AND P. COMTE, *Large-Eddy Simulations of Turbulence*, Cambridge University Press, 2005.
- [24] H. LIU, *Integrated modeling of insect flight: From morphology, kinematics to aerodynamics*, J. Comput. Phys., 228 (2009), pp. 439–459.
- [25] Q. LIU AND O. VASILYEV, *A Brinkman penalization method for compressible flows in complex*

- geometries*, J. Comput. Phys., 227 (2007), pp. 946–966.
- [26] M. MAEDA, N. GAO, N. NISHIHASHI, AND H. LIU, *A free-flight simulation of insect flapping flight*, J. Aero Aqua Bio-mech., 1 (2010), pp. 71–79.
 - [27] M. MAEDA AND H. LIU, *Ground effect in fruit fly hovering: A three-dimensional computational study*, J. Biomech. Sc. Engin., 8 (2013), pp. 344–355.
 - [28] R. MITTAL AND G. IACCARINO, *Immersed boundary methods*, Annu. Rev. Fluid Mech., 37 (2005), pp. 239–261.
 - [29] J. MORALES, W. BOS, K. SCHNEIDER, AND D. MONTGOMERY., *The effect of toroidicity on reversed field pinch dynamics*, Plasma Phys. Control. Fusion, 56 (2014), p. 095024.
 - [30] J. MORALES, M. LEROY, W. BOS, AND K. SCHNEIDER, *Simulation of confined magnetohydrodynamic flows using a pseudo-spectral method with volume penalization*, J. Comput. Phys., 274 (2014), pp. 64–94.
 - [31] N. MORDANT AND J.-F. PINTON, *Velocity measurement of a settling sphere*, Eur. Phys. J. B, 18 (2000), pp. 343–352.
 - [32] R. NGUYEN VAN YEN, D. KOLOMENSKIY, AND K. SCHNEIDER, *Approximation of the Laplace and Stokes operators with Dirichlet boundary conditions through volume penalization: A spectral viewpoint*, Numer. Math., 128 (2014), pp. 301–338.
 - [33] S. OSHER AND R. FEDKIW, *Level Set Methods and Dynamic implicit Surfaces*, Springer, 2003.
 - [34] D. PEKUROVSKY, *P3DFFT: a framework for parallel computations of Fourier transforms in three dimensions*, SIAM J. Sci. Computing, 34 (2012), pp. C192–C209.
 - [35] C. S. PESKIN, *The immersed boundary method*, Acta Numerica, 11 (2002), pp. 479–517.
 - [36] R. PEYRET, *Spectral Methods for Incompressible Viscous Flow*, Springer Berlin / Heidelberg, 2002.
 - [37] R. RAMAMURTI AND W. SANDBERG, *A computational investigation of the three-dimensional unsteady aerodynamics of drosophila hovering and maneuvering*, J. Exp. Biol.xp. Biol., 210 (2009), pp. 881–896.
 - [38] P. SCHLATTER, N. ADAMS, AND L. KLEISER, *A windowing method for periodic inflow/outflow boundary treatment of non-periodic flows*, J. Comput. Phys., 206 (2005), pp. 505–535.
 - [39] K. SCHNEIDER, *Numerical simulation of the transient flow behaviour in chemical reactors using a penalisation method*, Computers & Fluids, 34 (2005), pp. 1223–1238.
 - [40] K. SCHNEIDER, *Immersed boundary methods for numerical simulation of confined fluid and plasma turbulence in complex geometries: a review*, J. Plasma Phys., in press (2015).
 - [41] K. SCHNEIDER AND M. FARGE, *Numerical simulation of the transient flow behaviour in tube bundles using a volume penalization method*, J. Fluids Struct., 20 (2005), pp. 555–566.
 - [42] J. SCHULZE AND J. SESTERHENN, *Optimal distribution of porous media to reduce trailing edge noise*, Computers & Fluids, 78 (2013), pp. 41 – 53.
 - [43] K. SUZUKI, K. MINAMI, AND T. INAMURO, *Lift and thrust generation by a butterfly-like flapping wing-body model: immersed boundary-lattice Boltzmann simulations*, J. Fluid Mech., 767 (2015), pp. 659–695.
 - [44] J. F. THOMPSON, Z. WARSJI, AND C. W. MASTIN, *Numerical grid generation: Foundations and Applications*, North-Holland Amsterdam, 1985.
 - [45] M. UHLMANN, *An immersed boundary method with direct forcing for the simulation of particulate flows*, J. Comput. Phys., 209 (2005), pp. 448–476.